Environmental Science & Technology

Article

pubs.acs.org/est

Humic Acid Facilitates the Transport of ARS-Labeled Hydroxyapatite Nanoparticles in Iron Oxyhydroxide-Coated Sand

Dengjun Wang,[†,⊥] Scott A. Bradford,[‡] Ronald W. Harvey,[§] Bin Gao,[∥] Long Cang,[†] and Dongmei Zhou*[,†]

[†]Key Laboratory of Soil Environment and Pollution Remediation, Institute of Soil Science, Chinese Academy of Sciences, No. 71 East Beijing Road, Nanjing 210008, China

[‡]U.S. Salinity Laboratory, Agricultural Research Service, United States Department of Agriculture, 450 W. Big Springs Road, Riverside, California 92507, United States

[§]U.S. Geological Survey, 3215 Marine Street, Boulder, Colorado 80303, United States

[∥]Department of Agricultural and Biological Engineering, University of Florida, Gainesville, Florida 32611, United States

[⊥]Graduate School of the Chinese Academy of Sciences, Beijing 100049, China

Supporting Information

ABSTRACT: Hydroxyapatite nanoparticles (nHAP) have been widely used to remediate soil and wastewater contaminated with metals and radionuclides. However, our understanding of nHAP transport and fate is limited in natural environments that exhibit significant variability in solid and solution chemistry. The transport and retention kinetics of Alizarin red S (ARS)-labeled nHAP were investigated in water-saturated packed columns that encompassed a range of humic acid concentrations (HA, 0−10 mg L^{-1}), fractional surface coverage of iron oxyhydroxide coatings on sand grains (λ, 0−0.75), and pH (6.0−10.5). HA was found to have a marked effect on the electrokinetic properties of ARS-nHAP, and on the transport and retention of ARS-nHAP in granular media. The transport of ARS-nHAP was found to increase with increasing HA concentration because of enhanced colloidal stability and the reduced aggregate size. When HA = 10 mg L^{-1}, greater ARS-nHAP attachment occurred with increasing λ because of increased electrostatic attraction between negatively charged nanoparticles and positively charged iron oxyhydroxides, although alkaline conditions (pH 8.0 and 10.5) reversed the surface charge of the iron oxyhydroxides and therefore decreased deposition. The retention profiles of ARS-nHAP exhibited a hyperexponential shape for all test conditions, suggesting some unfavorable attachment conditions. Retarded breakthrough curves occurred in sands with iron oxyhydroxide coatings because of time-dependent occupation of favorable deposition sites. Consideration of the above effects is necessary to improve remediation efficiency of nHAP for metals and actinides in soils and subsurface environments.

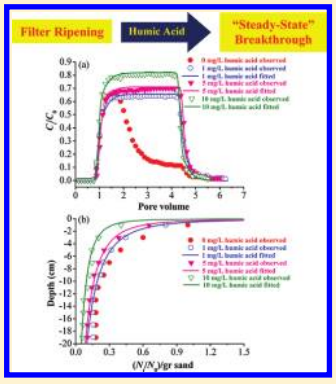

INTRODUCTION

Hydroxyapatite nanoparticle ($Ca_{10}(PO_4)_6(OH)_2$, nHAP), which is a biocompatible and bioactive ceramic,[1] has been widely advocated for use in remediation of metals in wastewater[2] and in nuclear waste disposal.[3] Metals (e.g., Pb, Sr, and Co) and actinides (e.g., U) can be sorbed onto the environmentally stable structure of nHAP.[2−4] However, little attention has been paid to the fate and transport of nHAP in soil and groundwater systems, even though nHAP has been suggested as a remediation agent for nuclear waste sites.[4] In addition, mobile nHAP can alter the distribution of many metal contaminants in soils and groundwater.[5,6] To track its transport and distribution in saturated granular media, nHAP was covalently bonded with the fluorescent label Alizarin red S (ARS), which is commonly used for histological staining of hydroxyapatite in mammalian embryos.[1,7]

Variability in soil structure, recharge rates, aqueous and solid phase geochemistry, and microbial community structure lead to physical heterogeneity and pH variability within soils.[8−11] These factors are known to influence the deposition of colloids, including nanoparticles (NPs), in granular media. Natural granular media exhibit surface charge heterogeneities characterized by microscale regions favorable to NP retention, even though average surface properties may be unfavorable.[8] Patches of iron and aluminum oxyhydroxides are common forms of surface charge heterogeneity that have been associated with enhanced NP retention. Unlike silica minerals, these metal oxyhydroxides are amphoteric with relatively high points of zero charge (pH_{PZC}). Often, pH values in groundwater and soils are below the pH_{PZC} of iron (7.5) and aluminum oxyhydroxides (9),[12] so these minerals acquire a net positive surface charge.[8,11] Because nHAP and silica exhibit a net negative charge at ambient pH,[6,13] nHAP attachment is expected to be "unfavorable" for silica and "favorable" for iron and aluminum oxyhydroxides. However, moderately to

Received: October 25, 2011
Revised: January 22, 2012
Accepted: February 9, 2012
Published: February 9, 2012

   dx.doi.org/10.1021/es203784u | Environ. Sci. Technol. 2012, 46, 2738−2745

highly alkaline conditions can result in reversal of surface charge of iron and aluminum oxyhydroxide coatings, thereby enhancing nHAP mobility.

Humic acid (HA), a major component of natural organic matter and ubiquitous in soils and groundwater environments, is one of the key factors governing the environmental transport and fate of colloids and especially NPs. For example, HA was found to enhance transport of nanosized C_{60} and carbon nanotubes in saturated porous media by decreasing electrostatic attraction and increasing steric repulsion.[14,15] However, the effect of HA on nHAP mobility in granular media has received only limited attention.[16] In particular, no research has yet been published on the influence of HA on nHAP mobility in the presence of variable amounts of iron oxyhydroxide coatings as a function of pH. The overall objective of this study was therefore to systemically investigate the roles of HA concentration, iron oxyhydroxide grain coatings, and pH on the transport of ARS-labeled nHAP in water-saturated packed columns.

MATERIALS AND METHODS

ARS-Labeled nHAP. nHAP (99+% purity) was obtained from Aipurui Nanomaterial, Inc., China. Detailed characterization of nHAP was conducted in our previous work.[16] Briefly, nHAP is 20 nm wide and 100 nm long, and has a Ca/P molar ratio of 1.65 and a specific surface area of 154 $m^2\ g^{-1}$. Alizarin red S (ARS, $C_{14}H_7NaO_7S$) was used as a label to facilitate tracking of nHAP through saturated, granular media. The ARS-labeled nHAP (ARS-nHAP) was prepared following the procedure reported elsewhere.[1] In brief, ARS (Sigma Aldrich, Germany) was dissolved in 0.1 M NaOH followed by addition of sonochemically synthesized nHAP. After 1 h, nHAP was pelleted by centrifugation (1000*g*), and then washed with ethanol and phosphate buffer.[17] Finally, ARS became irreversibly chemisorbed onto the surface of the nHAP by reacting with calcium.[17] Epifluorescence imaging of the ARS-nHAP was performed to confirm successful labeling by ARS (Figure S1 in Supporting Information).

Stable aqueous ARS-nHAP suspensions were prepared by adding 20 mg of ARS-nHAP powder to 200 mL of 0.1 mM NaCl solution at desired pH and HA concentration (see Table 1 and S2), stirring for 1 min, and sonicating (100 W, 45 kHz, KQ-300VDE sonicator, China) for 30 min at 25 °C to ensure a homogeneous suspension. The resulting suspension contained 100 mg L^{-1} ARS-nHAP.

Column Transport Experiments. Quartz sand (Sinopharm Chemical Reagent Co., Ltd., 0.55−0.65 mm, 0.6-mm median grain size[18]) served as the granular media in the column studies. Prior to use, the sand was cleaned thoroughly using a procedure described elsewhere.[18]

Three sets of column experiments were conducted to investigate the influence of HA on the transport and deposition of ARS-nHAP in saturated quartz sand. The first set investigated the effect of HA concentration (0, 1, 5, and 10 mg L^{-1}) in clean quartz sand at pH 7.2.

The second set was designed to investigate the effects of HA (10 mg L^{-1}) and surface charge heterogeneity, also at pH 7.2. Surface charge heterogeneity was introduced into our model granular media by coating a fraction of the grains with iron oxyhydroxides[8,11,19] following a procedure similar to that used by Stahl and James (S3).[20] Geochemically heterogeneous granular media were prepared by mixing portions of the coated and uncoated sand to achieve iron oxyhydroxide surface coverage ranging from λ = 0 to 0.75 (Table 1), where λ is the fraction of the quartz sand coated by iron oxyhydroxide.

Table 1. Electrokinetic Potentials of Sand Grain and ARS-nHAP, and Extended DLVO Parameters for the ARS-nHAP—Sand Interaction

HA[a] mg L^{-1}	IS[b] mM	λ[c]	pH	ζ_g[d] mV	$\zeta_{ARS\text{-}nHAP}$[e] mV	Φ_{max}[f] KT
0	0.1	0	7.2	−61.0 ± 1.3	−26.0 ± 2.5	67
1	0.1	0	7.2	−62.1 ± 1.2	−50.4 ± 3.7	250
5	0.1	0	7.2	−62.8 ± 1.4	−56.0 ± 3.5	307
10	0.1	0	7.2	−63.2 ± 2.1	−58.7 ± 1.8	355
10	0.1	0.075	7.2	−58.2 ± 1.4	−58.7 ± 1.8	292
10	0.1	0.150	7.2	−51.1 ± 0.8	−58.7 ± 1.8	259
10	0.1	0.225	7.2	−42.0 ± 1.7	−58.7 ± 1.8	218
10	0.1	0.300	7.2	−34.5 ± 1.5	−58.7 ± 1.8	180
10	0.1	0.375	7.2	−26.1 ± 2.1	−58.7 ± 1.8	145
10	0.1	0.750	7.2	−5.4 ± 0.7	−58.7 ± 1.8	107
10	0.1	0.150	6.0	−43.6 ± 2.9	−37.8 ± 2.7	156
10	0.1	0.150	8.0	−56.4 ± 3.1	−61.2 ± 2.1	296
10	0.1	0.150	10.5	−70.0 ± 1.4	−72.0 ± 2.3	423

[a]Humic acid (pH 7.2). [b]Ionic strength (NaCl as background electrolyte). [c]Fraction of the quartz grain surfaces coated by iron oxyhydroxide. [d]Zeta potential of quartz grain or average value of uncoated/coated quartz grain. [e]Zeta potential of ARS-nHAP. [f]Energy barrier to primary minimum as calculated by extended DLVO theory.

A third set of experiments examined the effect of pH on the transport of ARS-nHAP in sand having a heterogeneous surface charge at fixed surface coverage of iron oxyhydroxides (λ = 0.15) and HA concentration (10 mg L^{-1}) over a pH range of 6.0−10.5, where the latter pH exceeded the highest pH_{PZC} of the iron oxyhydroxides. The pH was adjusted using 1.0 mM HCl and/or NaOH to achieve pH values of 6.0, 8.0, and 10.5 (Table 1).

Transport experiments were conducted in 2.6-cm diameter, 20.0-cm long glass chromatography columns fitted on both ends with polytetrafluoroethene end-caps and stainless-steel mesh (80-μm openings). The columns were wet-packed using sequential 1-cm lifts. After each lift, the columns were tapped to eliminate air bubbles. In iron oxyhydroxide coating experiments, the coated/uncoated sand grains were thoroughly mixed to ensure an even distribution in the column. Porosity of the packed columns varied between 0.37 and 0.40.

To preclude desaturation, columns were run in an upflow mode using an YZΠ-15 peristaltic pump (Baoding Longer Precision Pump Co., Ltd., China) and equilibrated by sequentially pumping ∼10 pore volumes (PVs) of DI water followed by at least 10 PVs of the nHAP-free background electrolyte solution through the column at a constant Darcy velocity of 7.5×10^{-3} cm s^{-1}. A stable ARS-nHAP suspension (100 mg L^{-1}) with the same background electrolyte composition was then introduced into the column for about 4 PVs, followed by several PVs of background electrolyte solution (no ARS-nHAP) to flush any unattached NPs that were left in the column. Column effluent was collected using a BS-110A fraction collector (Huxi Analytical Instrument Factory Co., Ltd., China). The concentrations of ARS-nHAP in the effluent were determined spectrophotometrically at a wavelength of 518 nm (721-100, Jinghua Science and Technology Instrument Co., Ltd., China).[17] A calibration curve was constructed by diluting the 100 mg L^{-1} ARS-nHAP suspension, which was linear within the range of 0−100 mg L^{-1}.

Following the completion of each transport test, each column was dissected into 10 layers of 2-cm segments, and the collector grains in each fraction were extracted with DI water to determine spatial distribution profile of retained ARS-nHAP, as described earlier.[5,6] A mass balance was calculated by comparing the quantity of ARS-nHAP in the effluent and retained in the sands to that injected into the column. All transport tests were conducted at least in duplicate.

ARS-nHAP Aggregation and Electrokinetic Properties. Suspensions of ARS-nHAP (100 mg L^{-1}) were air-dried on 400-mesh, carbon-coated Cu transmission electron microscopy (TEM) grids. The morphology, structure, and size of individual ARS-nHAP were then measured using TEM (JEOL TEM-2100). The average ARS-nHAP aggregate size and the intrinsic size distributions in various influent and select effluent suspensions were determined by dynamic light scattering (DLS) measurement, which are given in S4.

To better understand the mechanisms governing ARS-nHAP transport and deposition in saturated sand, ARS-nHAP was characterized under the same conditions as those employed in the column experiments described below. Electrophoretic mobilities were obtained using microelectrophoresis (Zhongcheng Digital Technology model JS94G, China) at room temperature, as described ealier,[16,18] and converted to zeta (ζ) potentials using the Smoluchowski equation.[21] Streaming potentials of the iron oxyhydroxide-coated sand grains were measured[22] using a streaming potential analyzer (BI-EKA, Brookhaven Instruments Corp., Holtsville, NY) and converted to ζ-potentials using the Helmholtz−Smoluchowski equation.[21] This zeta potential information was used in conjunction with extended Derjaguin−Landau−Verwey−Overbeek (DLVO) theory[23,24] to calculate the average interaction energy of ARS-nHAP with the various granular media (S5).

Data Analysis. A one-dimensional form of the advection−dispersion equation with two-site kinetic retention was used to simulate the ARS-nHAP transport and retention.[25,26] The first kinetic site assumes reversible, time-dependent retention using first-order retention (k_1) and detachment (k_{1d}) coefficients, and a Langmuirian type blocking function[27] to account for filling of the "reversible binding sites" on the grain surfaces as the solid phase ARS-nHAP concentration approaches s_{max1}. The second kinetic site assumes irreversible retention using a first-order retention coefficient (k_2) and a depth-dependent blocking function.[25] Details on the mathematical model, including operative equations, are given in S6.

RESULTS AND DISCUSSION

Electrokinetic Properties of ARS-nHAP and Sand Grain. The ζ-potentials of the ARS-nHAP and the sand grains under the different experimental conditions are shown in Table 1. The results indicate both the ARS-nHAP and quartz sand are negatively charged over the tested range of HA concentration and pH conditions, consistent with previous results.[6,16,28] The ARS-nHAP is more negatively charged than unlabeled nHAP (−26.0 vs −17.1 mV) due to the presence of hydroxyl and carbonyl functional groups on the ARS.[17] The ζ-potential increased from −26.0 to −58.7 mV in response to increases in HA concentration from 0 to 10 mg L^{-1} because of HA sorption onto the ARS-nHAP.[28] The magnitude of the ζ-potential increased with suspension pH due to dissociation of proton groups on the ARS-nHAP and quartz sand.[21]

As expected, ζ-potential estimated from streaming potentials for the mixture of uncoated and iron oxyhydroxide-coated sand grains at pH 7.2 became considerably less negative as λ increased from 0 to 0.75. Consistent with previous findings,[8,19] ζ-potential for the sand mixtures was the algebraic sum of the ζ-potential for the clean and iron oxyhydroxide-coated fractions (Figure S7), after correcting for λ.

Properties of the ARS-nHAP. The measured average particle sizes of ARS-nHAP in the absence and presence of HA are provided in Table 2. The intensity-weighted hydrodynamic size measured by DLS for ARS-nHAP in the influent was dependent on the HA concentration, ranging from 275 to 343 nm. The ARS-nHAP size decreased with increasing HA concentration, indicating that HA increased the stability of the ARS-nHAP suspension as a result of the decrease in ζ-potential (Table 1). In contrast, the average sizes of individual ARS-nHAP measured by TEM were in the vicinity of 100 nm (Table 2). The intensity-weighted hydrodynamic diameter was used in the DLVO calculations because it is more relevant to Brownian transport of the ARS-nHAP than the diameter determined by TEM.

Table 2. Sizes of ARS-nHAP

ARS-nHAP	HA mg L^{-1}	DLS size[a] nm	TEM size[b] nm
influent[c]	0	343 ± 11	101 ± 2.5
	1	306 ± 9.2	101 ± 1.6
	5	301 ± 8.4	101 ± 1.8
	10	275 ± 9.1	101 ± 1.3
effluent[c]	0	252 ± 7.5	100 ± 1.4
	1	235 ± 9.6	99.5 ± 1.2
	5	203 ± 7.3	99.7 ± 1.4
	10	185 ± 8.9	100 ± 1.8

[a]Average intensity-weighted hydrodynamic particle size of ARS-nHAP, determined by DLS measurement. [b]Average particle size of ARS-nHAP was determined by TEM measurement. [c]Ionic strength was adjusted to be 0.1 mM of NaCl for all HA concentrations.

Effect of HA. Figure 1a and 1b present breakthrough curves (BTCs) and retention profiles (RPs), respectively, of ARS-nHAP being advected through quartz sand at pH 7.2 in the presence of 0, 1, 5, and 10 mg L^{-1} HA (in the range of environmental relevant HA concentration).[29] The BTCs are plotted as dimensionless concentration C_i/C_0 of ARS-nHAP as a function of PVs. The RPs are plotted as normalized concentration (quantity of the ARS-nHAP recovered in the sand, N_t, divided by the C_0) per gram of dry sand as a function of distance from the column inlet. The corresponding mass recovery of ARS-nHAP in the effluent and sand is shown in Table 3. Because virtually all (99.8−104%) of the ARS-nHAP was recovered, there is a high degree of confidence in the experimental procedures.

HA was found to have a marked effect on the extent of ARS-nHAP transport and aggregation. Total ARS-nHAP recovery increased from 30.5 to 63.4, to 70.2, and to 78.8% when HA concentration was increased from 0 to 1, to 5, and to 10 mg L^{-1}, respectively (Figure 1a and Table 3). Interestingly, the BTC in the absence of HA suggested ripening behavior, i.e., increasing deposition rate with time, indicative of ARS-nHAP aggregation on the solid phase. Examples of particle-size distributions of the ARS-nHAP in the absence and presence of HA are presented in Figure 2 and Table 2. The addition of HA was found to stabilize the ARS-nHAP suspension and thereby reduce substantially the size of ARS-nHAP in both the column influent and effluent samples. For the influent, particle size

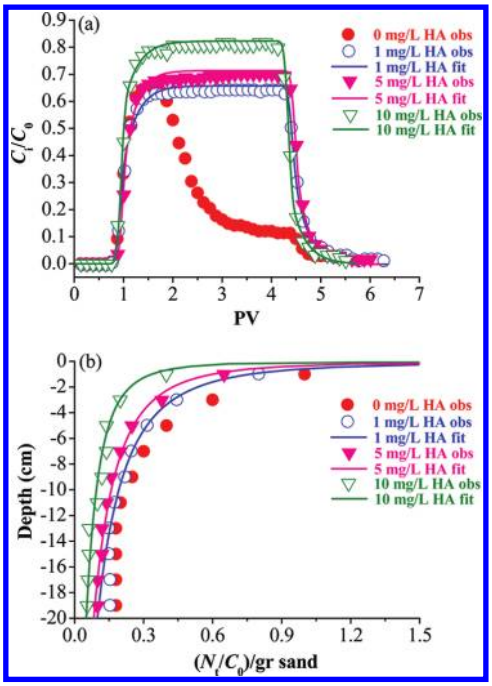

Figure 1. Measured and fitted breakthrough curves (a) and retention profiles (b) for ARS-nHAP under different concentrations of humic acid (HA) at pH 7.2 in quartz sand. Fitted curves were obtained using the two-site kinetic attachment model. In (b) the normalized concentration (quantity of the ARS-nHAP recovered in the sand, N_t, divided by C_0) per gram of dry sand and these are plotted as a function of the distance from the column inlet.

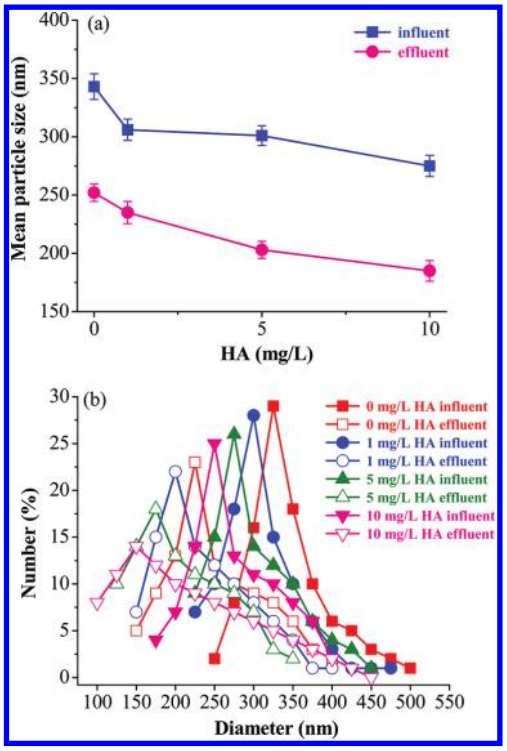

Figure 2. Mean intensity-weighted hydrodynamic size of influent and effluent of ARS-nHAP (a) determined by DLS for different suspension concentrations of HA and (b) the corresponding particle size distribution (pH 7.2).

decreased steadily from 343 to 275 nm in response to increases in HA from 0 up to 10 mg L^{-1}, respectively. Sizes of ARS-nHAP in the effluent also decreased steadily (from 252 to 185 nm) with increasing HA, but were always smaller than those in the influent due to the size-selective effect of the granular media. Comparison of the TEM photomicrographs (Figure 3) further revealed that larger ARS-nHAP aggregates dissociated into smaller ones in the presence of HA. These observations indicate that, in the absence of HA, ARS-nHAP aggregates were more efficiently removed during transport. This could be due to greater degree of ripening, higher collision efficiency due to sedimentation and interception because of a larger effective particle size, or more likely to a combination of both.[30]

The ζ-potential of ARS-nHAP also became more negative with increasing HA. Calculations based upon DLVO theory indicate that this alteration of the surface properties enhanced the height of the primary energy barrier for both aggregation in solution and subsequent attachment to grain surfaces (Table 1). Consequently, disaggregation (Figures 2 and 3) and less retention (Figure 1) of ARS-nHAP occurred at higher HA concentrations because of increased electrostatic repulsions. Similarly, Xie et al.[14] attributed disaggregation of C_{60} to changes in surface charge with adsorption of HA.

Table 3. Mass Balance Percentages for ARS-nHAP in Saturated Packed Column Experiments at Varying HA Concentration, Iron Oxyhydroxide Grain Coating, and pH

HA mg L^{-1}	IS mM	λ	pH	M_{eff}[a] %	M_{ret}[b] %	$M_{ret\text{-}inlet}$[c] %	M_{tot}[d] %
0	0.1	0	7.2	30.5 ± 1.3	69.5 ± 1.1	46.2 ± 1.9	100 ± 2.4
1	0.1	0	7.2	63.4 ± 1.6	36.4 ± 1.3	42.1 ± 1.1	99.8 ± 2.9
5	0.1	0	7.2	70.2 ± 2.1	30.1 ± 1.4	38.5 ± 1.3	100 ± 3.5
10	0.1	0	7.2	78.8 ± 1.9	24.9 ± 1.2	34.7 ± 0.8	104 ± 3.1
10	0.1	0.075	7.2	56.8 ± 2.1	41.1 ± 3.1	38.8 ± 1.1	97.9 ± 5.2
10	0.1	0.150	7.2	53.7 ± 2.3	42.5 ± 3.2	39.1 ± 0.9	96.2 ± 5.5
10	0.1	0.225	7.2	49.4 ± 2.5	44.3 ± 3.5	39.3 ± 0.8	93.7 ± 6.0
10	0.1	0.300	7.2	46.5 ± 2.2	44.8 ± 3.7	39.5 ± 0.7	91.3 ± 5.9
10	0.1	0.375	7.2	43.6 ± 2.3	45.9 ± 4.1	39.7 ± 1.2	89.5 ± 6.4
10	0.1	0.750	7.2	38.7 ± 3.2	48.2 ± 4.5	41.2 ± 1.1	86.9 ± 7.7
10	0.1	0.150	6.0	49.1 ± 1.5	51.2 ± 1.4	47.7 ± 1.2	100 ± 2.9
10	0.1	0.150	8.0	67.4 ± 2.1	35.6 ± 1.2	42.3 ± 0.9	103 ± 3.3
10	0.1	0.150	10.5	69.8 ± 1.2	29.7 ± 1.1	41.7 ± 1.0	99.5 ± 2.3

[a]Refers to the effluent percentage of ARS-nHAP recovered from column tests. [b]Refers to the retained percentage of ARS-nHAP recovered from column tests. [c]Refers to the ARS-nHAP retained near the column inlet. [d]Refers to the total percentage of ARS-nHAP recovered from column tests.

dx.doi.org/10.1021/es203784u | Environ. Sci. Technol. 2012, 46, 2738–2745

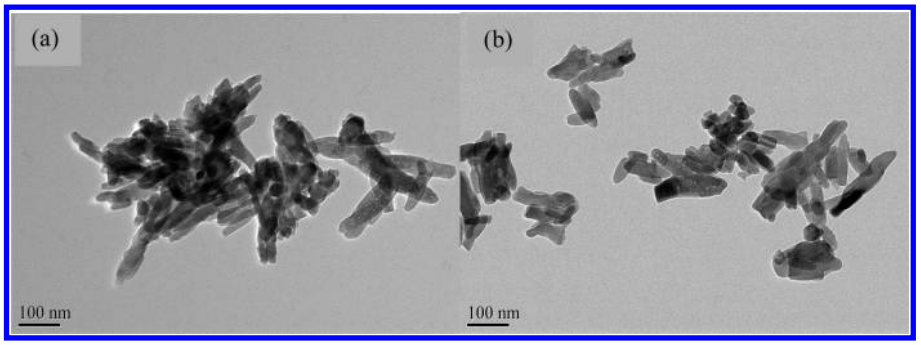

Figure 3. Representative TEM micrographs of ARS-nHAP in the absence (a) and presence (b) of 10 mg L^{-1} HA.

Table 4. Fitted Parameters of the Two-Site Kinetic Attachment Model As Estimated from the Breakthrough Data for Saturated Packed Column at Varying HA Concentration, Iron Oxyhydroxide Grain Coating, and pH

HA mg L^{-1}	IS mM	λ	pH	k_1[a] min^{-1}	k_{1d}[b] min^{-1}	k_2[c] min^{-1}	s_{max1}/C_0[d] $(N_t/C_0)/g$	R^2[e]
0	0.1	0	7.2	NA	NA[f]	NA	NA	NA
1	0.1	0	7.2	2.09×10^{-02}	1.24×10^{-01}	1.07×10^{-01}	NA	0.995
5	0.1	0	7.2	1.54×10^{-02}	1.13×10^{-01}	7.77×10^{-02}	NA	0.994
10	0.1	0	7.2	1.05×10^{-02}	9.96×10^{-02}	4.66×10^{-02}	NA	0.996
10	0.1	0.075	7.2	8.92×10^{-02}	NA	1.00×10^{-02}	2.10×10^{-02}	0.991
10	0.1	0.150	7.2	9.50×10^{-02}	NA	1.08×10^{-02}	2.71×10^{-02}	0.989
10	0.1	0.225	7.2	1.05×10^{-01}	NA	2.16×10^{-02}	3.08×10^{-02}	0.991
10	0.1	0.300	7.2	1.14×10^{-01}	NA	3.05×10^{-02}	3.61×10^{-02}	0.983
10	0.1	0.375	7.2	1.20×10^{-01}	NA	3.52×10^{-02}	4.12×10^{-02}	0.993
10	0.1	0.750	7.2	1.22×10^{-01}	NA	1.35×10^{-01}	1.48×10^{-01}	0.992
10	0.1	0.150	6.0	1.04×10^{-01}	NA	5.91×10^{-02}	9.87×10^{-02}	0.991
10	0.1	0.150	8.0	5.92×10^{-02}	NA	7.71×10^{-03}	2.93×10^{-02}	0.989
10	0.1	0.150	10.5	5.25×10^{-02}	NA	1.78×10^{-03}	1.44×10^{-02}	0.988

[a]First-order retention coefficient on site 1. [b]First-order detachment coefficient on site 1. [c]First-order retention coefficient on site 2. [d]Maximum solid phase concentration of ARS-nHAP on site 1 normalized by the input ARS-nHAP concentration. [e]Squared Person's correlation coefficient. [f]Not applicable.

In contrast with classical filtration theory[30] which predicts exponential loss with depth, the RPs of ARS-nHAP typically exhibited a hyperexponential shape with greater retention in the section adjacent to the column inlet (0–4 cm) and rapidly decreasing retention with depth (Figure 1b). Hyperexponential profiles were more pronounced at lower HA concentrations. Approximately 34.7% of the retained ARS-nHAP occurred near the column inlet when the HA concentration was 10 mg L^{-1}, whereas the value was as high as 46.2% in the absence of HA (Table 3).

The two-site kinetic retention model provided a good description for both BTCs and RPs when the [HA] > 0, judging from the high correlation coefficients reported in Table 4. Values of kinetic model parameters k_1, k_{1d}, and especially k_2 decreased with increasing HA concentration. This observation suggests that mechanisms controlling ARS-nHAP retention near the column inlet were more sensitive to the HA concentration. Because the model did not account for ripening, it was not employed to describe the data collected in the absence of HA.

Effects of Iron Oxyhydroxide Grain Coatings. Figure 4a and b presents BTCs and RPs, respectively, for ARS-nHAP in various mixtures of uncoated and iron oxyhydroxide-coated quartz sand (λ = 0, 0.075, 0.150, 0.225, 0.300, 0.375, and 0.750) at pH 7.2 in the presence of 10 mg L^{-1} HA. The corresponding mass recoveries of ARS-nHAP from the effluent and from the sand are shown in Table 3. In contrast to experiments examining the influence of HA, the total mass balance for ARS-nHAP became progressively poorer (104 to 86.9%) as λ increased. Iron oxyhydroxide surfaces exhibit a strong positive charge (31.9 mV) at pH 7.2, which is below the estimated pH_{PZC} of 8.4 (Figure S8). Consequently, ARS-nHAP can be strongly (and much less reversibly) sorbed in the primary minimum.

Surface charge heterogeneity was found to have a marked effect on the transport of ARS-nHAP (Figure 4a). The ARS-nHAP breaks through at progressively later times and has lower amounts of ARS-nHAP in the effluent as λ increases (M_{eff} = 78.8 to 38.7%, Table 3). These observations reflect the larger fraction of the surface area that is favorable (iron oxyhydroxide) for ARS-nHAP attachment (or ARS-nHAP/HA cosorption). In particular, the amount of attachment is proportional to λ. Similarly, the amount of time required for ARS-nHAP to occupy the most favorable attachment sites increases with λ. Only after the sites associated with the iron oxyhydroxides are occupied can substantive breakthrough start to occur.

Figure 4b shows the RPs for ARS-nHAP as a function of λ. The RPs do not reflect the complete mass of ARS-nHAP in the sand for larger values of λ because of the strong ARS-nHAP retention on the iron oxyhydroxide-coated sand that was not completely recovered during extraction (Table 3). Nevertheless, the amount of ARS-nHAP retention clearly increased with λ as expected from the BTCs (Figure 4a) and the hyperexponential shape of the RPs (Figure 1b). These results indicate that the RPs still provide useful information in a more qualitative sense. The fractional retention of ARS-nHAP

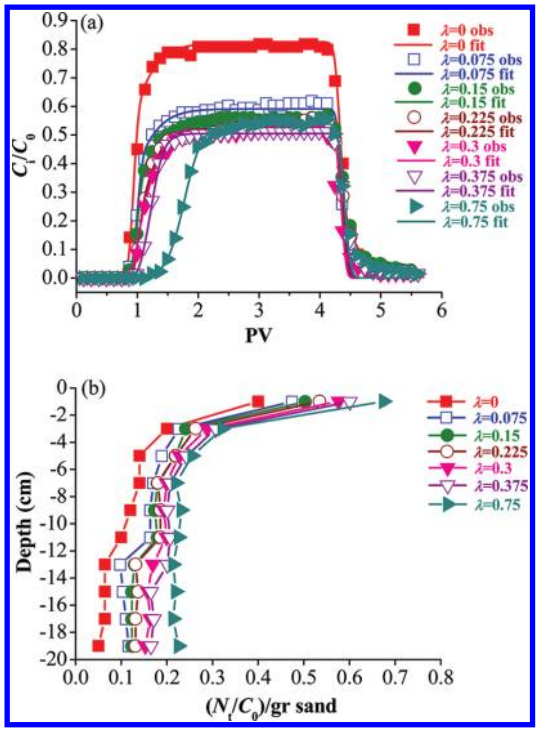

Figure 4. Measured and fitted breakthrough curves (a) and measured retention profiles (b) for ARS-nHAP under different iron oxyhydroxide coating fraction conditions (λ) at pH 7.2 in the presence of 10 mg L^{-1} HA. Fitted curves were obtained using the two-site kinetic attachment model. In (b) the normalized concentration (quantity of the ARS-nHAP recovered in the sand, N_t, divided by C_0) per gram of dry sand and these are plotted as a function of the distance from the column inlet.

($M_{ret}^{ARS\text{-}nHAP}$) increased about 2-fold when λ was increased from 0 to 0.75, which was substantially smaller than the retained mass of nHAP at a similar amount of iron oxyhydroxide-coated sand (M_{ret}^{nHAP} increased 2.8-fold when λ increased from 0 to 0.36).[6] This observation suggests that the HA is masking much of the positive charged sites on the iron oxyhydroxides. To confirm this hypothesis, we measured streaming potentials of the iron oxyhydroxide-coated sand after equilibration with different concentrations of HA (0, 5, and 10 mg L^{-1}). Interestingly, its ζ-potential increased from −51.1 to −62.3, and then to −66.5 mV when the equilibration suspension HA concentration increased from 0 to 5, and then to 10 mg L^{-1}. This observation confirms that HA acts as a masking agent, and thereby reduces the deposition of ARS-nHAP by decreasing the net positive charge of the iron oxyhydroxide-coated sand.

The two-site kinetic retention model was used to simulate the BTCs for the various uncoated/coated sand mixtures. Table 4 provides optimized values of k_1, k_2, and s_{max1}, as well as the correlation coefficients (R^2). The BTCs were well described using this model (Figure 4a). Values of k_1, k_2, and s_{max1} tended to increase with λ. This trend is expected because s_{max1} is proportional to the fraction of the surface area that is favorable for retention.[31−33] The colloid sticking efficiency is proportional to k_1 and has been reported to exhibit a one-to-one correspondence with the surface coverage of metal oxyhydroxides[8,19] in the absence of HA. However, in this work, the colloid sticking efficiency (α) was found to increase substantively less (from 0.033 to 0.124) than predicted when λ was increased from 0 to 0.75, respectively, in the presence of 10 mg L^{-1} HA. This observation further indicates that HA is acting to "mask" much of the positive charge on the iron oxyhydroxide-coated sand grains.

Effect of pH. Figure 5a and 5b present BTCs and RPs, respectively, for ARS-nHAP in a mixture of uncoated and iron

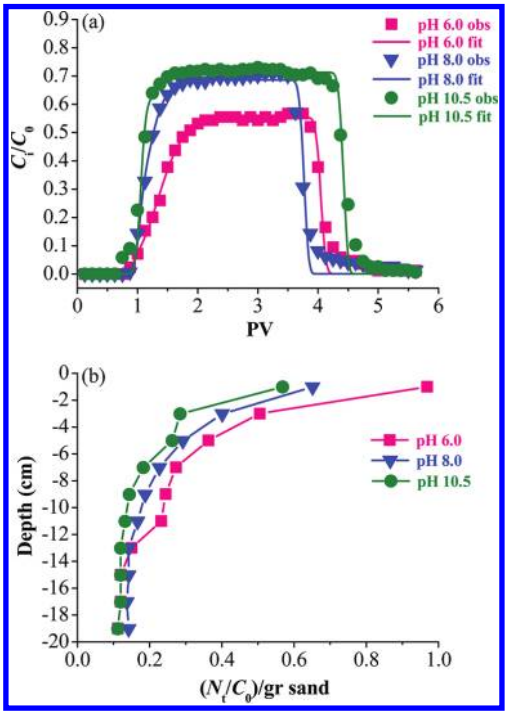

Figure 5. Measured and fitted breakthrough curves (a) and measured retention profiles (b) for ARS-nHAP under the indicated pH conditions in a mixture of uncoated and iron oxyhydroxide-coated quartz sand (λ = 0.15, where λ is the fraction of the quartz grain surfaces coated by iron oxyhydroxide) in the presence of 10 mg L^{-1} HA. Fitted curves were obtained using the two-site kinetic attachment model. In (b) the normalized concentration (quantity of the ARS-nHAP recovered in the sand, N_t, divided by C_0) per gram of dry sand and these are plotted as a function of the distance from the column inlet.

oxyhydroxide-coated quartz sand (λ = 0.15) in the presence of 10 mg L^{-1} HA and varied pH (6.0, 8.0, and 10.5). Corresponding mass recovery of ARS-nHAP in the effluent and sand (Table 3) indicated good (99.5−103%) mass balances under these conditions. The nanoparticles broke through at progressively earlier times and, as expected, were subject to lower degrees of attenuation (M_{eff} increased from 49.1 to 69.8%) as the pH increased. These observations are consistent with more of a quartz-dominated system at lower λ and relatively high concentrations of HA. Increasing pH to 10.5 is sufficient to reverse the surface charge of the iron oxyhydroxide coating. Thus, electrostatic repulsion between the negatively charged ARS-nHAP and sand grains was dominant in promoting the mobility of the ARS-nHAP at suspension pH 10.5, consistent with observations reported by Ryan et al.[9,10] Increasing pH had a similar effect as increasing HA concentration on ARS-nHAP transport behavior. As pH increased, the surface charges of the nanoparticles, quartz grains, and iron oxyhydroxide patches became more negative. This causes the energy barrier to attachment in the primary

dx.doi.org/10.1021/es203784u | Environ. Sci. Technol. 2012, 46, 2738−2745

minimum to increase, resulting in less retention (more transport) (Table 1).

The hyperexponential shape of the ARS-nHAP RPs (Figure 5b) became less pronounced at higher pH. For example, about 47.7% of the total retention occurred near the column inlet at pH 6.0, in contrast to 41.7% at pH 10.5 (Table 3). This is due, in part, to enhanced ARS-nHAP aggregation at lower pH. Similar results were observed in our previous work.[6]

The two-site kinetic retention model again provided reasonable fits for the BTCs (see Figure 5a and optimized values of k_1, k_2, and s_{max1} in Table 4). Values of k_1, k_2, and s_{max1} all decreased with increasing pH. These observations indicate that ARS-nHAP retention on both sites 1 and 2 depended on the strength of the adhesive interaction (e.g., secondary minimum) which decreases with increasing pH.

Mechanisms of ARS-nHAP Retention. Wang et al.[6] investigated the mechanisms of nHAP (absence of ARS) retention for different values of pH and λ, but in the absence of HA. In brief, nHAP retention was demonstrated to depend on nHAP aggregation, chemical heterogeneity, and surface roughness when $\lambda = 0$. Furthermore, conditions were demonstrated to be favorable for nHAP attachment on iron oxyhydroxide-coated sand grains when $\lambda > 0$ at pH 6.2. The influence of these same factors is investigated below for ARS-nHAP in the presence of HA.

Mechanisms of ARS-nHAP retention are expected to be similar to that for nHAP under comparable attachment conditions. In the present study, calculated energy barriers to the primary minimum in the presence of HA and pure quartz sand were less favorable for attachment of ARS-nHAP (Table 1) relative to nHAP in earlier studies.[5,6] Similar factors seem to be affecting deposition of ARS-nHAP and nHAP in these sets of studies. Information presented in S9 of the Supporting Information confirms the substantial effect of surface roughness[34−38] on ARS-nHAP retention under these conditions. The importance of ARS-nHAP aggregation on retention was already demonstrated in Figures 2 and 3 and Table 2.

Environmental Implications. The present study highlights several implications for nHAP application to soils and groundwater environments. In the absence of NOM (e.g., HA), nHAP has only limited transport capacity due to its high surface area and large tendency to aggregate. However, a very small amount of HA (e.g., 1 mg L^{-1}) can substantially enhance its mobility in saturated granular media. In aquifer sediments, where substantive amounts of iron oxyhydroxide can be present on grain surfaces, large quantities of nHAP attachment may occur because of favorable electrostatic attraction between nanoparticles and collector surfaces. However, NOM clearly diminishes attachment due to partial masking of the positive charge on iron oxyhydroxide surfaces. In addition, nanoparticle attachment is further decreased under more alkaline conditions (pH 8.0 and 10.5) due to charge reversal on iron oxyhydroxide surfaces.

Hyperexponential RPs occurred during all of the considered experimental conditions. These observations suggest that hyperexponential RPs are a general phenomenon associated with attachment under unfavorable conditions, and not necessarily associated with a single retention mechanism. Unfavorable conditions for deposition are common in subsurface environments because of heterogeneities in both chemistry of the pore water and surface chemistry of the grains. Based upon our current studies using model media, considerable variability in the attenuation of nHAP in the subsurface may be expected because of local variability in pH, HA concentration, and surface coverage of iron oxyhydroxides. However, additional research is needed to determine more accurately the contributions of these parameters on the transport behaviors of nHAP and other nanoparticles in more complex media typical of natural soils and aquifer sediments.

■ ASSOCIATED CONTENT

Supporting Information

Additional materials and methods, additional results, and data pertaining to the epifluorescence micrographs (Figure S1); HA stock solution (S2); coating the sand grain (S3); DLS measurements (S4); extended DLVO theory (S5); mathematical model (S6); ζ-potential of heterogeneous sand grains (Figure S7); pH_{PZC} of iron-coated sand (Figure S8); and surface roughness on ARS-nHAP retention (S9). This material is available free of charge via the Internet at http://pubs.acs.org.

■ AUTHOR INFORMATION

Corresponding Author

*E-mail: dmzhou@issas.ac.cn; phone: +86-25-86881180; fax: +86-25-86881000.

Notes

The authors declare no competing financial interest.

■ ACKNOWLEDGMENTS

We acknowledge financial support from the National Natural Science Foundation of China (41125007) and Open Fund of the State Key Laboratory of Soil and Sustainable Agriculture (Y052010027). Any use of trade, firm, or product names is for descriptive purposes only and does not imply endorsement by the United States government.

■ REFERENCES

(1) Vukomanovic, M.; Zavasnik-Bergant, T.; Bracko, I.; Skapin, S. D.; Ignjatovic, N.; Radmilovic, V.; Uskokovic, D. Poly(D,L-lactide-*co*-glycolide)/hydroxyapatite core-shell nanospheres. Part 3: Properties of hydroxyapatite nano-rods and investigation of a distribution of the drug within the composite. *Colloids Surf., B* **2011**, *87* (2), 226−235.

(2) Ma, Q. Y.; Traina, S. J.; Logan, T. J.; Ryan, J. A. Effects of aqueous Al, Cd, Cu, Fe(II), Ni, and Zn on Pb immobilization by hydroxyapatite. *Environ. Sci. Technol.* **1994**, *28* (7), 1219−1228.

(3) Oelkers, E. H.; Montel, J. M. Phosphates and nuclear waste storage. *Elements* **2008**, *4* (2), 113−116.

(4) Handley-Sidhu, S.; Renshaw, J. C.; Moriyama, S.; Stolpe, B.; Mennan, C.; Bagheriasl, S.; Yong, P.; Stamboulis, A.; Paterson-Beedle, M.; Sasaki, K.; Pattrick, R. A. D.; Lead, J. R.; Macaskie, L. E. Uptake of Sr^{2+} and Co^{2+} into biogenic hydroxyapatite: Implications for biomineral ion exchange synthesis. *Environ. Sci. Technol.* **2011**, *45* (16), 6985−6990.

(5) Wang, D. J.; Paradelo, M.; Bradford, S. A.; Peijnenburg, W.; Chu, L. Y.; Zhou, D. M. Facilitated transport of Cu with hydroxyapatite nanoparticles in saturated sand: Effects of solution ionic strength and composition. *Water Res.* **2011**, *45* (18), 5905−5915.

(6) Wang, D. J.; Bradford, S. A.; Paradelo, M.; Peijnenburg, W.; Zhou, D. M. Facilitated transport of copper with hydroxyapatite nanoparticles in saturated sand. *Soil Sci. Soc. Am. J.* **2011**, *76* (2), doi: 10.2136/sssaj 2011.0203.

(7) Williams, T. W. Alizarin red S and toluidine blue for differentiating adult or embryonic bone and cartilage. *Stain Technol.* **1941**, *16* (1), 23−25.

(8) Johnson, P. R.; Sun, N.; Elimelech, M. Colloid transport in geochemically heterogeneous porous media: Modeling and measurements. *Environ. Sci. Technol.* **1996**, *30* (11), 3284−3293.

(9) Ryan, J. N.; Elimelech, M.; Ard, R. A.; Harvey, R. W.; Johnson, P. R. Bacteriophage PRD1 and silica colloid transport and recovery in an iron oxide-coated sand aquifer. *Environ. Sci. Technol.* **1999**, *33* (1), 63−73.
(10) Ryan, J. N.; Harvey, R. W.; Metge, D.; Elimelech, M.; Navigato, T.; Pieper, A. P. Field and laboratory investigations of inactivation of viruses (PRD1 and MS2) attached to iron oxide-coated quartz sand. *Environ. Sci. Technol.* **2002**, *36* (11), 2403−2413.
(11) Abudalo, R. A.; Harvey, R. W.; Metge, D. W.; Landkamer, L.; Ryan, J. N. Influence of organic matter on the transport of *Cryptosporidium parvum* oocysts in a ferric oxyhydroxide-coated quartz sand saturated porous medium. *Water Res.* **2010**, *44* (4), 1104−1113.
(12) Parks, G. A. Isoelectric points of solid oxides solid hydroxides and aqueous hydroxo complex systems. *Chem. Rev.* **1965**, *65* (2), 177−198.
(13) Petosa, A. R.; Jaisi, D. P.; Quevedo, I. R.; Elimelech, M.; Tufenkji, N. Aggregation and deposition of engineered nanomaterials in aquatic environments: Role of physicochemical interactions. *Environ. Sci. Technol.* **2010**, *44* (17), 6532−6549.
(14) Xie, B.; Xu, Z. H.; Guo, W. H.; Li, Q. L. Impact of natural organic matter on the physicochemical properties of aqueous C_{60} nanoparticles. *Environ. Sci. Technol.* **2008**, *42* (8), 2853−2859.
(15) Hyung, H.; Fortner, J. D.; Hughes, J. B.; Kim, J. H. Natural organic matter stabilizes carbon nanotubes in the aqueous phase. *Environ. Sci. Technol.* **2007**, *41* (1), 179−184.
(16) Wang, D. J.; Chu, L. Y.; Paradelo, M.; Peijnenburg, W.; Wang, Y. J.; Zhou, D. M. Transport behavior of humic acid-modified nano-hydroxyapatite in saturated packed column: Effects of Cu, ionic strength, and ionic composition. *J. Colloid Interface Sci.* **2011**, *360* (2), 398−407.
(17) Moriguchi, T.; Yano, K.; Nakagawa, S.; Kaji, E. Elucidation of adsorption mechanism of bone-staining agent alizarin red S on hydroxyapatite by FT-IR microspectroscopy. *J. Colloid Interface Sci.* **2003**, *260* (1), 19−25.
(18) Zhou, D. M.; Wang, D. J.; Cang, L.; Hao, X. Z.; Chu, L. Y. Transport and re-entrainment of soil colloids in saturated packed column: Effects of pH and ionic strength. *J. Soils Sed.* **2011**, *11* (3), 491−503.
(19) Elimelech, M.; Nagai, M.; Ko, C. H.; Ryan, J. N. Relative insignificance of mineral grain zeta potential to colloid transport in geochemically heterogeneous porous media. *Environ. Sci. Technol.* **2000**, *34* (11), 2143−2148.
(20) Stahl, R. S.; James, B. R. Zinc sorption by iron-oxide-coated sand as a function of pH. *Soil Sci. Soc. Am. J.* **1991**, *55* (5), 1287−1290.
(21) Elimelech, M.; Gregory, J.; Jia, X.; Williams, R. A. *Particle deposition and aggregation: Measurement, modeling and simulation*; Butterworth-Heinemann: Oxford, U.K., 1995.
(22) Johnson, P. R. A comparison of streaming and micro-electrophoresis methods for obtaining the zeta potential of granular porous media surfaces. *J. Colloid Interface Sci.* **1999**, *209* (1), 264−267.
(23) Derjaguin, B.; Landau, L. Theory of the stability of strongly charged lyophobic sols and of the adhension of strongly charged particles in solutions of electrolytes. *Acta Physicochim. URSS* **1941**, *14*, 733−762.
(24) Verwey, E. J. M.; Overbeek, J. T. G. *Theory of the Stability of Lyophobic Colloids*; Elsevier: Amsterdam, The Netherlands, 1948.
(25) Bradford, S. A.; Simunek, J.; Bettahar, M.; van Genuchten, M. T.; Yates, S. R. Modeling colloid attachment, straining, and exclusion in saturated porous media. *Environ. Sci. Technol.* **2003**, *37* (10), 2242−2250.
(26) Schijven, J. F.; Simunek, J. Kinetic modeling of virus transport at the field scale. *J. Contam. Hydrol.* **2002**, *55* (1−2), 113−135.
(27) Adamczyk, Z.; Siwek, B.; Zembala, M.; Belouschek, P. Kinetics of localized adsorption of colloid particles. *Adv. Colloid Interface Sci.* **1994**, *48*, 151−280.
(28) Chu, L. Y.; Wang, D. J.; Wang, Y. J.; Si, Y. B.; Zhou, D. M. Transport behavior of hydroxyapatite nanoparticles in saturated packed column: Effects of humic acid, pH, and ionic strength. *Environ. Sci. (in Chinese)* **2011**, *32* (8), 2284−2291.
(29) Redman, A. D.; Macalady, D. L.; Ahmann, D. Natural organic matter affects arsenic speciation and sorption onto hematite. *Environ. Sci. Technol.* **2002**, *36* (13), 2889−2896.
(30) Yao, K. M.; Habibian, M. M.; O'Melia, C. R. Water and waste water filtration: Concepts and applications. *Environ. Sci. Technol.* **1971**, *5* (11), 1105−1112.
(31) Chen, J. Y.; Ko, C. H.; Bhattacharjee, S.; Elimelech, M. Role of spatial distribution of porous medium surface charge heterogeneity in colloid transport. *Colloids Surf., A* **2001**, *191* (1−2), 3−15.
(32) Torkzaban, S.; Tazehkand, S. S.; Walker, S. L.; Bradford, S. A. Transport and fate of bacteria in porous media: Coupled effects of chemical conditions and pore space geometry. *Water Resour. Res.* **2008**, *44* (4), doi:10.1029/2007WR006541.
(33) Torkzaban, S.; Bradford, S. A.; Walker, S. L. Resolving the coupled effects of hydrodynamics and DLVO forces on colloid attachment in porous media. *Langmuir* **2007**, *23* (19), 9652−9660.
(34) Shellenberger, K.; Logan, B. E. Effect of molecular scale roughness of glass beads on colloidal and bacterial deposition. *Environ. Sci. Technol.* **2002**, *36* (2), 184−189.
(35) Hoek, E. M. V.; Bhattacharjee, S.; Elimelech, M. Effect of membrane surface roughness on colloid-membrane DLVO interactions. *Langmuir* **2003**, *19* (11), 4836−4847.
(36) Yoon, J. S.; Germaine, J. T.; Culligan, P. J. Visualization of particle behavior within a porous medium: Mechanisms for particle filtration and retardation during downward transport. *Water Resour. Res.* **2006**, *42* (6), doi:10.1029/2004WR003660.
(37) Morales, V. L.; Gao, B.; Steenhuis, T. S. Grain surface-roughness effects on colloidal retention in the vadose zone. *Vadose Zone J.* **2009**, *8* (1), 11−20.
(38) Shen, C. Y.; Li, B. G.; Wang, C.; Huang, Y. F.; Jin, Y. Surface roughness effect on deposition of nano- and micro-sized colloids in saturated columns at different solution ionic strengths. *Vadose Zone J.* **2011**, *10* (3), 1071−1081.